SCIENTIFIC REPORTS

OPEN

SUBJECT AREAS:
MECHANICAL PROPERTIES
THEORY AND COMPUTATION
PHYSICS
FERROELECTRICS AND MULTIFERROICS

Received
16 May 2012

Accepted
9 October 2012

Published
12 November 2012

Correspondence and requests for materials should be addressed to Y.Z. (zhengy35@mail.sysu.edu.cn) or B.W. (wangbiao@mail.sysu.edu.cn)

# Vortex Domain Structure in Ferroelectric Nanoplatelets and Control of its Transformation by Mechanical Load

W. J. Chen[1,2], Yue Zheng[1,2] & Biao Wang[1,2]

[1]State Key Laboratory of Optoelectronic Materials and Technologies, Sun Yat-sen University, Guangzhou 510275, China, [2]School of Physics and Engineering, Sun Yat-sen University, Guangzhou 510275, China.

**Vortex domain patterns in low-dimensional ferroelectrics and multiferroics have been extensively studied with the aim of developing nanoscale functional devices. However, control of the vortex domain structure has not been investigated systematically. Taking into account effects of inhomogeneous electromechanical fields, ambient temperature, surface and size, we demonstrate significant influence of mechanical load on the vortex domain structure in ferroelectric nanoplatelets. Our analysis shows that the size and number of dipole vortices can be controlled by mechanical load, and yields rich temperature-stress (T-S) phase diagrams. Simulations also reveal that transformations between "vortex states" induced by the mechanical load are possible, which is totally different from the conventional way controlled on the vortex domain by the electric field. These results are relevant to application of vortex domain structures in ferroelectric nanodevices, and suggest a novel route to applications including memories, mechanical sensors and transducers.**

Nanoscale ferroelectrics and multiferroics have been actively investigated for many years. Nanoscale ferroelectrics and multiferroics often retain bulk properties, and even exhibit enhanced or novel properties including electronic, optoelectronic, electrochemical, electromechanical and magnetoelectric, properties, due to effects of finite size, surfaces and interfaces. Therefore, nanoscale ferroelectrics and multiferroics play important roles in the fabrication and miniaturization of nanoscale functional devices[1-9]. More recently, exotic ferroelectric domain structures described as topological defects in the polarization field have attracted an enormous amount of attention due to their fundamental scientific interest and potential applications in domain engineering[10–28]. In particular, toroidal polarization patterns consisting of flux-closure domains (so-called vortex domain structures) are found in low-dimensional ferroelectrics with extreme geometric confinement. As a new kind of polarization ordering, vortex domain structures are expected to exhibit distinctive characteristics and novel coupling with external fields, which could open exciting opportunities in designing novel nano-memories, sensors and transducers, and other devices. Nevertheless, experimental and theoretical studies for the vortex domain structures in low-dimensional ferroelectrics have proved to be difficult, and properties determined by the vortex domain structures in low-dimensional ferroelectric materials are presently poorly understood.

Existence of vortex domain structures has been predicted in some low-dimensional ferroelectric nanostructures based on theoretical simulations[10–12,21]. In addition, some experimental studies have made great steps towards unambiguous observation of nanoscale polarization vortices[14,18,25,26]. While it is of fundamental and technological importance to characterize vortex domain structures in low-dimensional ferroelectrics, it is even more important to develop methods to control the vortex domain structures in low-dimensional ferroelectrics. Several theoretical investigations have focused on control of the vortex domain structures in low-dimensional ferroelectrics through external electromechanical fields[29–36]. Using the effective Hamiltonian method, Ponomareva et al.[29] investigated effects of the electric boundary condition and epitaxial strain on the dipole pattern of $Pb(Zr_{0.4}Ti_{0.6})O_3$ nanodots and wires. Combining simulations and an analytical model, Prosandeev and Bellaiche[30] studied the characteristics and signatures of dipole vortices in ferroelectric nanodots. Mechanisms of vortex switching, vortex rotation and vortex-to-polarization transformation induced by various kinds of electric fields in ferroelectric nanostructures were also investigated by effective Hamiltonian simulations[31–35]. Using phase-field simulation, vortex switching under curled electric field in ferroelectric nanostructures has also been

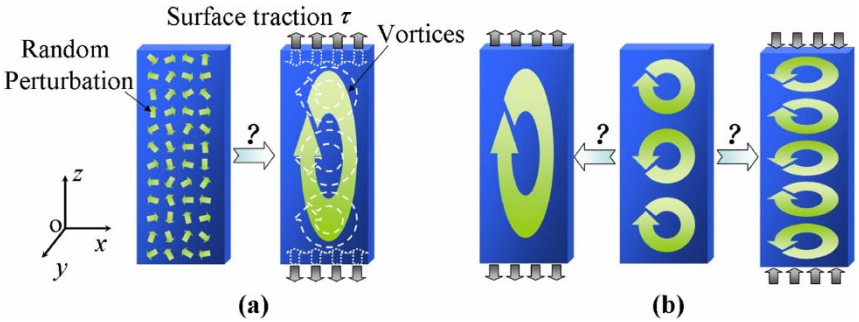


**Figure 1 | Schematics of the simulated nanosystems.** A ferroelectric nanoplatelet under different surface traction along its prolate direction with (a) initial random polarization perturbation or (b) initial vortex domain structure.

investigated[36]. These works provide useful information on how to detect and control vortex domain structures in ferroelectric nanostructures.

The effect of mechanical strains and stresses on polarization and polarization-related properties in ferroelectrics and multiferroics is well known[4–10]. In contrast, investigations of the mechanical load effect on the vortex domain structures in low-dimensional ferroelectrics and multiferroics are scarce[10,29,37]. In general, it is expected that the size, number and orientation of dipole vortices should be affected by mechanical load. In order to exploit the coupling between the vortex domain structure and mechanical loads in applications, a number of questions must be answered, including how mechanical load affects the formation and stability of vortex domain structures, and whether mechanical-load-controlled transformations between different "vortex states" are possible.

In this work, in order to understand the effect of the mechanical load on stability and structure of the vortex domain in nanoscale ferroelectrics, we present a theoretical investigation of the vortex domain structure in three-dimensional ferroelectric nanoplatelets (FNPL) with careful consideration of the effects of inhomogeneous electromechanical fields, ambient temperature, surfaces, size, and other factors. Systematic phase-field simulations are conducted to explore effects of an external mechanical load on the evolution and equilibrium of vortex domain structures in nanoplatelets. We calculate temperature-stress (T-S) phase diagrams, and depict vortex domain structure as a function of mechanical load and ambient temperature. By considering different initial polarization distributions in nanoplatelets, transformations between different "vortex states" induced by mechanical load are demonstrated, and dynamic features during the transformations are also revealed.

## Results

**Vortex domain structure in free-standing FNPL.** We consider prolate $PbTiO_3$ nanoplatelet under open-circuit electric condition in our simulations. The initial polarization distribution of the nanoplatelet is either a random polarization perturbation or a vortex domain structure as shown in Fig. 1. By controlling the surface traction $\tau$ at the top and bottom surfaces, evolution of the spontaneous polarization $\mathbf{P}$ in FNPL under tensile or compressive mechanical load along the prolate direction (i.e., $z$-direction) can be simulated based on the phase-field method. The toroidal moment, i.e., $\mathbf{g}=\frac{1}{V}\int_V \mathbf{r}\times(\mathbf{P}-\bar{\mathbf{P}})\mathrm{d}V$, is adopted to characterize the vortex domain structure. Here $V$ is the volume of the system, $\mathbf{r}$ is the position vector, and $\bar{\mathbf{P}}$ is the mean spontaneous polarization of the system[13]. To confine the toroidal moment along $y$-direction, a three-dimensional $10\Delta x\times 3\Delta y\times 30\Delta z$ meshing at a scale of $\Delta x=\Delta y=\Delta z=1$ nm is employed. Results obtained in our simulations are not only confined to this simple perovskite. Similar effects should be found in other ferroelectric materials such as $BaTiO_3$, $Ba_xSr_{1-x}TiO_3$ and $Pb(Zr_xTi_{1-x})O_3$, etc., which are also predicted to adopt vortex domain structures in low-dimensional nanostructures.

We start with an investigation on the vortex domain structure of a free-standing nanoplatelet. Simulations of polarization evolution at various temperatures from up to $10^2$ sets of initial random perturbations are conducted to find the possible vortex domain structures. The random perturbations obey the normal distribution with zero mean polarization and standard deviation being $10^{-4}Cm^{-2}$. Simulated results indicate that multiple "vortex states" (i.e., vortex domain structures with different size and number of vortices, or toroidal direction) are stable in the free-standing nanoplatelet, especially at low temperature. As shown in Fig. 2, "vortex states" with up to three dipole vortices are generally observed at $T = 0$K. It can be seen that the vortices lie in the $x$-$z$ plane due to the strongest confinement in $y$-dimension, and manifest with near-null $x$- and $z$-components of the toroidal moment. Tracing the evolution of toroidal moment and domain morphologies as shown in Fig. 2, we classify three typical behaviors during the formation of vortex domain structure, i.e., nucleation, growth and adjustment. At the beginning, dipole vortices nucleate to decrease the high energy density caused by strong polarization inhomogeneity. After that, the vortices grow rapidly and generally lead to a sudden increase of toroidal moment. During the evolution, the vortices keep adjusting their sizes to balance each

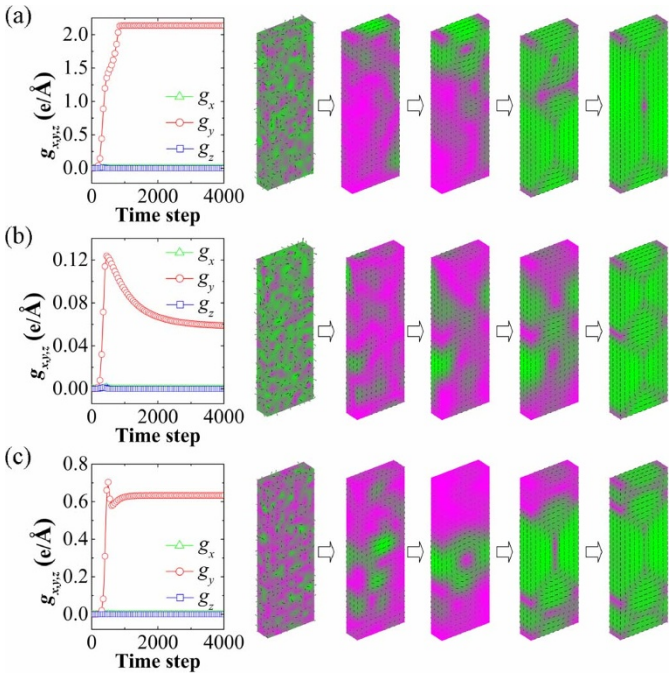


**Figure 2 | Evolution of the toroidal moment and domain morphology in a free-standing nanoplatelet.** Toroidal moment evolution and snapshots of domain evolution from different initial random perturbations towards equilibrium (a) 1-vortex, (b) 2-vortices and (c) 3-vortices states.

other, and some of them may be extruded out or merge into a bigger one (e.g., see Fig. 2a).

**Mechanical-load-controlling vortex domain structure of FNPL.** The multiplicity of stable vortex domain structures in low-dimensional ferroelectric nanostructures indicates an uncertainty of achieving specific "vortex state", which also shows some potential applications, such as developing multiple-bits memory unit. The key that brings such multiplicity to application is an efficient control of vortex domain structure through external loads. Considering the interaction between polarization and mechanical stress field, regular controllability of the vortex domain structure by mechanical load is also possible. In order to summarize this behavior, we further simulate the vortex domain structure of a nanoplatelet under different surface traction with the initial random perturbation as shown in Fig. 2a. For a nanoplatelet under different surface traction $\tau$, evolution of the $y$-component of toroidal moment $g_y$ is shown in Fig. 3a at room temperature ($T$=300K). The initial and equilibrium domain morphologies are also depicted in the inserts. It can be seen that the equilibrium vortex domain structure is obviously dependent on the surface traction. As $\tau$ takes values from –2.0 GPa to 0 GPa by a step of 0.1 GPa, simulations show that the equilibrium vortex domain structures have five vortices at $\tau \in [-2.0\ \text{GPa}, -1.1\ \text{GPa}]$, four vortices at $\tau \in [-1.0\ \text{GPa}, -0.7\ \text{GPa}]$, three vortices at $\tau \in [-0.6\ \text{GPa}, -0.4\ \text{GPa}]$, and one vortex at $\tau \in [-0.3\ \text{GPa}, 0\ \text{GPa}]$, respectively. Meticulously tracing the domain morphologies evolutions, we can find that mechanical load significantly affects the nucleation and balance of vortices and thus results in various equilibrium vortex domain structures (see Supplementary Fig. S1 on line).

As ambient temperature is able to affect the weights of free energy components and the stability of vortex domain structure (see Supplementary Fig. S2 on line), the mechanical load effect on the vortex domain structure in nanoplatelet is expected to be dependent on temperature. In Fig. 3b and 3c, we depict respectively the simulated mean magnitude of polarization over all sites, i.e., $\langle P\rangle \equiv \text{mean}\left(\sqrt{P_1^2+P_2^2+P_3^2}\right)$, and the $y$-component of toroidal moment $g_y$ of equilibrium domain structure as functions of surface traction $\tau$ at different temperatures. For each given temperature, it can be seen in Fig. 3b and 3c that the mean magnitude of polarization and the toroidal moment have strong dependence on surface traction, where abrupt change at some values indicates different vortex domain structures. At the same time, effect of temperature is also particularly important to the mean magnitude of polarization and the toroidal moment. For a given vortex domain structure, it can be found that the increase of temperature tends to decrease the mean magnitude of polarization and toroidal moment. Besides, the abrupt positions are also changed along the axis of surface traction with variation of temperature as shown in Fig. 3b and 3c, which indicates that the existing ranges of specific vortex domain structures are significantly dependent on temperature.

More importantly, in order to clearly investigate the common influence of mechanical load and temperature on the vortex domain structure in FNPL, we depict the temperature-stress (T-S) phase diagram (as shown in Fig. 3d) of equilibrium vortex domain structure according to the results shown in Fig. 3b and 3c. As shown in Fig. 3d, we obtain six different equilibrium vortex domain structures in a nanoplatelet under the combining effects of mechanical load and temperature. In general, the nanoplatelet tends to adopt vortex domain structures with more/fewer vortices at more compressive/tensile surface traction. Note that the nanoplatelet with large compressive surface traction adopts vortex domain structures with four or five vortices. However, these domain structures are difficult to obtain from random perturbations in a free-standing nanoplatelet. After removing the surface traction, vortex domain structures with more vortices may remain stable or destabilize into those with fewer

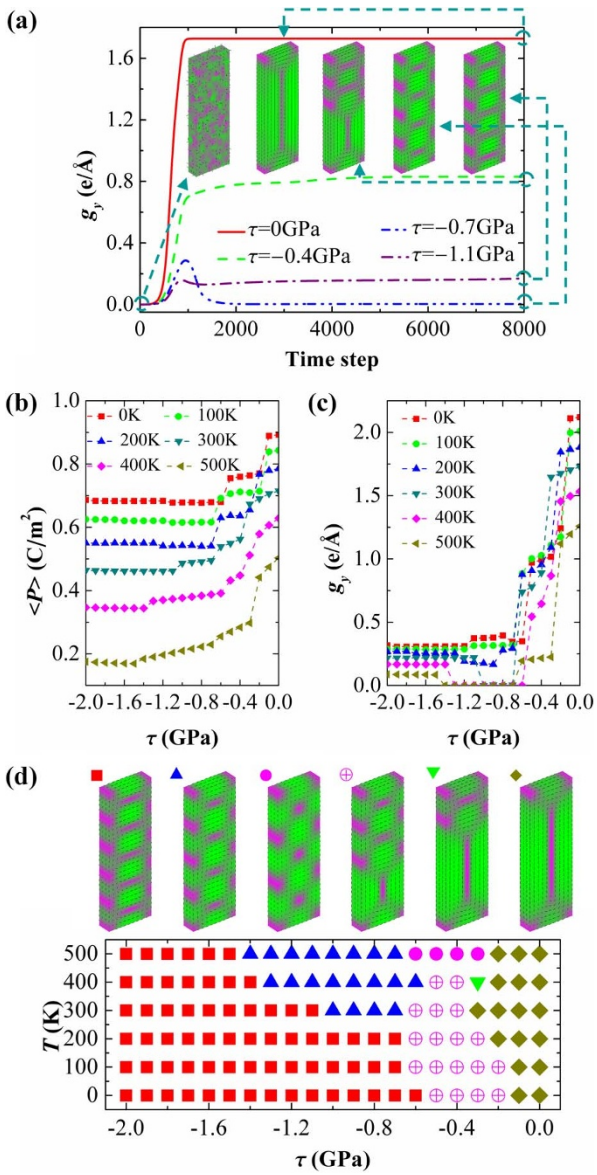


**Figure 3 | Mechanical load effect on a nanoplatelet with initial random perturbation.** A nanoplatelet is under various mechanical loads but with a given initial random perturbation as that shown in Fig. 2a. (a) The evolution of the toroidal moment component $g_y$ under different surface traction at $T$=300 K. The inserts depict the initial and equilibrium domain morphologies. (b) and (c) depict the mean polarization magnitude and the toroidal moment component of equilibrium vortex domain structure as functions of surface traction under given temperatures. (d) Phase diagram of the equilibrium vortex domain structure as a function of surface traction and temperature.

vortices, which is also strongly dependent on the temperature (see Supplementary Fig. S3a on line). Therefore, combining effects of temperature and mechanical load, we can find the rich vortex domain structures in a ferroelectric nanoplatelet.

**Mechanical-load-controlling transformation of vortex domain structure in FNPL.** While the above results demonstrate strong effect of mechanical load on formation of vortex domain structure, it is of particular significance to investigate the response of existing vortex domain structures to mechanical load, and to confirm that mechanical-load-controlling transformations between "vortex states" are possible. To the best knowledge of us, such kind of vortex transformation has not yet been predicted for three-dimensional

ferroelectric nanostructures. In order to find the relationship between mechanical load and transformation of vortex domain structure, simulations of a nanoplatelet under different surface traction are conducted in following investigation.

The simulated results of a nanoplatelet with initial 1-vortex state are shown in Fig. 4. According to the evolution of toroidal moment together with the inserted initial and equilibrium domain morphologies (Fig. 4a), it can be seen that the mechanical load indeed can induce transformations between "vortex states". In this case, the initial 1-vortex state is compressed into 3-vortices state at –1.3 Gpa and into 5-vortices state at –1.8 Gpa at room temperature, manifested with a significant decrease of the equilibrium toroidal

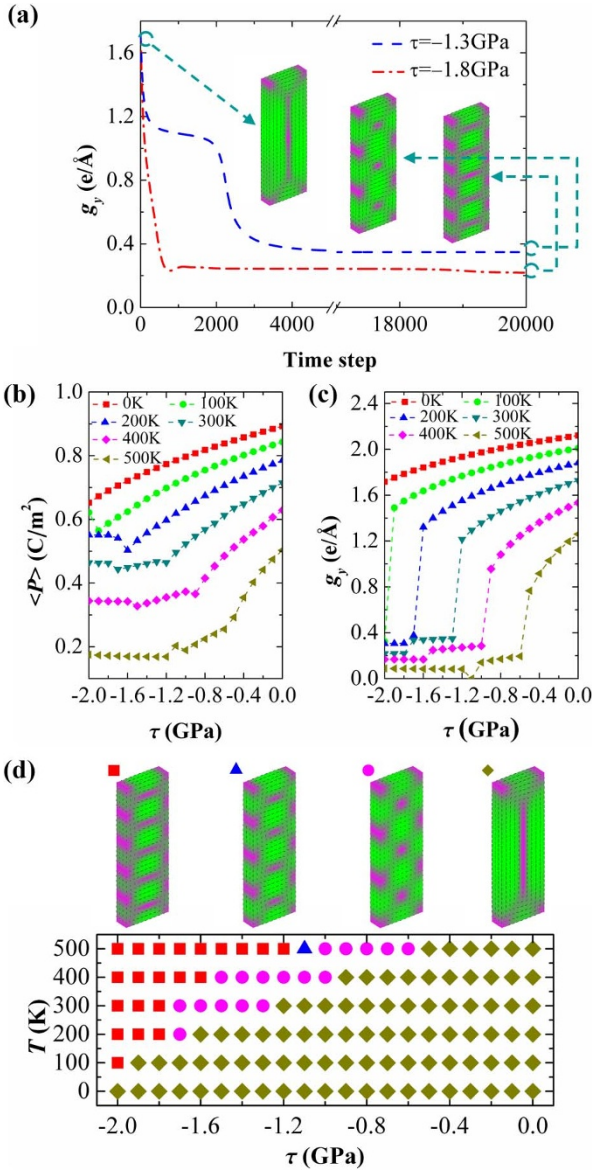


**Figure 4 | Mechanical load effect on a nanoplatelet with initial 1-vortex state.** A nanoplatelet is under various mechanical loads but with an initial 1-vortex state obtained at free-standing condition. (a) The evolution of the toroidal moment component $g_y$ under different surface traction $T$=300 K. The inserts depict the initial and equilibrium domain morphologies. (b) and (c) depict the mean polarization magnitude $<P>$ and the toroidal moment component $g_y$ of equilibrium vortex domain structure as functions of surface traction under given temperatures. (d) Phase diagram of the equilibrium vortex domain structure as a function of surface traction and temperature.

moment. As what we will discuss later in this section, the above transformations are accomplished by nucleation of new vortices at the core of initial vortices or at the surfaces of nanoplatelet.

To clearly study the effect of mechanical load on vortex domain structure in FNPL, the equilibrium mean magnitude of polarization and the toroidal moment are simulated as functions of surface traction at different temperatures (Fig. 4b and 4c). At $T$ = 0K, the mean magnitude of polarization and the toroidal moment decrease smoothly with increasing magnitude of surface traction from 0 to 2.0 GPa. At higher temperature, abrupt changes of the two quantities as function of surface traction are observed, indicating that transformations of the initial 1-vortex state into other "vortex states". Similar to the result of a nanoplatelet with initial random perturbation (see Fig. 3), the abrupt positions have strong dependences on the temperature. From the calculated T-S phase diagram as shown in Fig. 4d, it can be seen that these abrupt changes correspond to transformations of the initial 1-vortex state into "vortex states" with three, four and five vortices, respectively. Increasing temperature tends to decrease magnitude of the minimum transforming surface traction. For example, for transformation from 1-vortex state to 3-vortices state, the minimum compression surface traction changes from −1.7 GPa to −0.6 GPa with the increase of temperature from 100 K to 500 K. This indicates that ambient temperature can significantly affect the transforming barrier of the "vortex states". Moreover, the domain structures with more vortices may remain stable or destabilize into other ones with fewer vortices, and the transformations are also dependent on temperature (see Supplementary Fig. S3b on line).

For a nanoplatelet with initial 2-vortices state (note, the vortices are in similar size as that shown in Fig. 2b), the effect of mechanical load is further investigated. Fig. 5a depicts the evolution of toroidal moment at room temperature, where the initial 2-vortices state is compressed into domain structures with four and six vortices at $\tau$=−1.7 GPa and −1.9 GPa, respectively, and it can be also stretched into 1-vortex state when $\tau$ reaches 1.3 GPa. Combining effects of mechanical load and temperature, we also calculate the mean magnitude of polarization, the toroidal moment, and the corresponding T-S phase diagram. The results are shown in Fig. 5b and 5c. Note that the investigated temperature is no higher than 300 K, as the 2-vortices state for a FNPL with free-standing condition is unstable when temperature is higher than about 330 K. Compared with the case of initial 1-vortex state, transformations of 2-vortices state into "vortex states" with more vortices seem more difficult, since nucleation of new vortices at the core of smaller vortex or at the surfaces is more difficult. In the investigated range of surface traction, no transformation is observed at $T$ = 0 K and $T$ = 100 K. Nevertheless, transformation from 2-vortices state to 4-vortices state is observed at $T$ = 200 K, and that from 2-vortices state to 6-vortices state is also found possible at $T$ = 300 K. Furthermore, transformation of 2-vortices state to 1-vortex state can be induced by a tensile surface traction at room temperature, yet appears in a not very regular way as shown in Fig. 5c. Our simulations show that this transformation happens only with the surface traction $\tau$ between 1.3 GPa and 1.5 GPa. According to the vortex domain structure in Fig. 5c, we attribute this stable 2-vortices state to the similar size of the two vortices, which easily leads to a balance of the two vortices under range of our analyzed stress load. For the initial 2-vortices state with vortices in distinct size, or for the initial 3-vortices state, their transformations into 1-vortex state are much easier to be induced by tensile surface traction (see Supplementary Fig. S4 on line).

In view of the above results, we would like to investigate the evolutions of mechanical-load-controlling transformations between "vortex states". At room temperature, Fig. 6a and 6b depict evolutions of a nanoplatelet with initial 2-vortices state transforming into 4-vortices state at $\tau$=−1.7 GPa and 1-votex state at $\tau$=1.4 GPa, respectively. Results of other different kinds of transformations can be found in

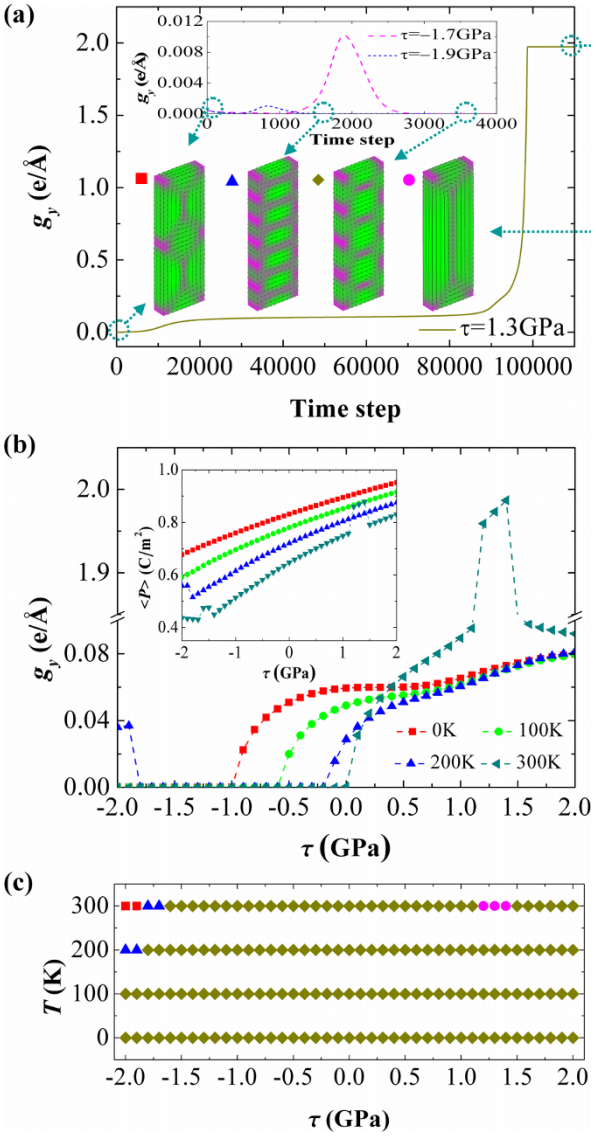


**Figure 5 | Mechanical load effect on a nanoplatelet with initial 2-vortices state.** A nanoplatelet is under various mechanical loads but with an initial 2-vortices state obtained at free-standing condition. (a) The evolution of the toroidal moment component $g_y$ under different surface traction $T=300$ K. The inserts depict the initial and equilibrium domain morphologies. (b) and (c) depict the mean polarization magnitude and the toroidal moment component $g_y$ of equilibrium vortex domain structure as functions of surface traction under given temperatures. (d) Phase diagram of the equilibrium vortex domain structure as a function of surface traction and temperature.

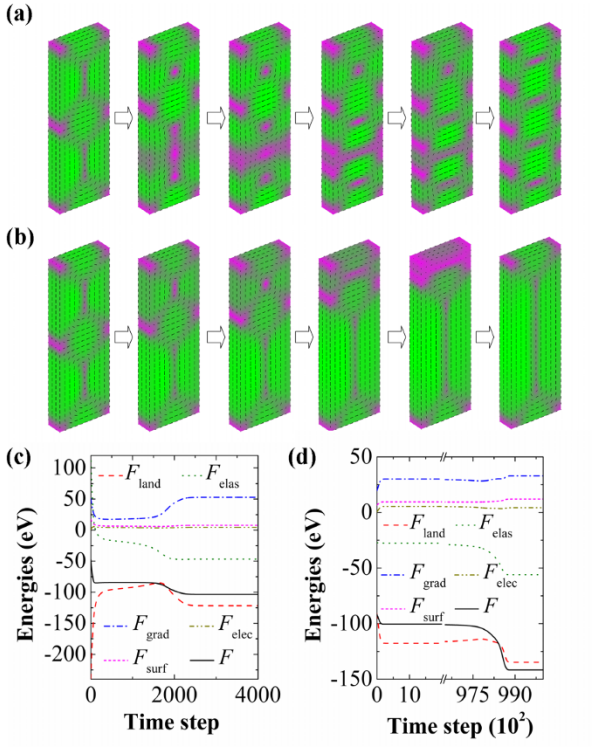


**Figure 6 | Evolution of the domain morphology and free energies during transformations of vortex states.** Snapshots of the domain evolution during (a) the transformation from 2-vortices state to 4-vortices state under compressive loading $\tau=-1.7$ GPa and (b) the transformation from 2-vortices state to 1-vortex state under tensile loading $\tau=1.3$ GPa at $T=300$ K. (c) and (d) depict the corresponding evolutions of the free energy and its components during the two transformations, respectively.

Supplementary Fig. S5 on line. For the 2-vortices to 4-vortices transformation as shown in Fig. 6a, it can be seen that new vortices nucleate at the core of the initial vortex. In general, through this way, the initial big vortex evolves into $(2n+1)$ small vortices, with $n$ being the integer. Transformations such as 2-vortices state to 6-vortices state, 1-vortex state to 3-vortices state and 1-vortex state to 5-vortices state are all through this mechanism. It should be noted that vortex nucleation at the surface is also possible (e.g., transformation from 1-vortex state to 4-vortices state as shown in Supplementary Fig. S5 on line). As depicted by Fig. 6b, under influence of tensile traction, the transformation from 2-vortices state to 1-vortex state is fulfilled by the squeezing out of one vortex. This squeezing out mechanism is more likely to happen when the initial vortices have different size. Otherwise, the vortices may fall into a balance that is difficult to break.

Tracing the evolution of the free energies as shown in Fig. 6c and 6d, it can be seen that the transformations are driven by decreasing of the total free energy of the system. The elastic energy, Landau energy and gradient energy contribute most of the total free energy, and they change significantly during transformations of the vortex domain structures. Meanwhile, the electric energy and surface energy remain small levels but also change a little bit. For the transformation from 2-vortices state to 4-vortices state shown in Fig. 6a, as compressive mechanical load acts on the nanoplatelet, the elastic energy contributed by the coupling of compressive stress and $z$-directed polarization is relatively large, and causes a depressing of $z$-polarization domains. This is accompanied by increase of the Landau energy and decrease of the gradient free energy. Vortex nucleation takes place as the decrease of elastic and gradient energy overwhelms the increase of Landau energy. At this point, local depolarization field should play an important role in vortex nucleation. After that, the Landau energy decreases and the gradient free energy increases significantly due to the growth of new vortices. For transformation from 2-vortices state to 1-vortex state, the evolutions of the free energies indicate different features. In this case (see Fig. 6d), the decrease of total free energy is more significant, which is mainly driven by the decrease of elastic energy and Landau energy. The squeezing out of one vortex induced by the tensile loading increases the magnitude of polarization quite an amount, and results in large decrease of elastic energy and Landau energy, but also an increase of gradient energy. Nevertheless, despite the large thermodynamic driving force, the transformation from 2-vortices state to 1-vortex state takes a much longer simulating time than that from 2-vortices state to 4-vortices state, which indicates a larger kinetic barrier.

## Discussion

Our simulations demonstrate significant effects of mechanical load on the vortex domain structure and its transformation in ferroelectric nanoplatelet. Results show that the size and number of dipole vortices in the domain structure of ferroelectric nanoplatelet can be regularly controlled by adjusting the mechanical load, and yields rich temperature-stress (T-S) phase diagrams of vortex domain structure. Vortex domain structures with more/fewer vortices can be generally obtained by applying compressive/tensile mechanical load to the ferroelectric nanoplatelet. Consequently, the toroidal moment of the nanoplatelet and the polarization magnitude of the dipoles exhibit remarkable controllability. As an important finding, our calculations demonstrated that the mechanical-load-controlling transformations between different "vortex states" are possible, which are totally different from those conventionally controlled on the vortex domain by external electric fields. The regular controllability of vortex domain structure and control of its transformation by mechanical load are believed common in nanoscale ferroelectrics adopting vortex domain structures. At the same time, results in present work should be relevant for applications exploiting the vortex domain structure of nanoscale ferroelectrics.

Nevertheless, we only have considered nanoplatelets with a special size and shape under open-circuit condition in present work. According to configuration of the ferroelectric nanoplatelets, the direction of the toroidal moment is strongly fixed along the *y*-axis, thus mechanical load mostly affect the magnitude of toroidal moment by changing the size and number of vortices and the polarization magnitude of dipoles. Actually, for other ferroelectric nanostructures, such as nanodots and nanorods, not only the magnitude but also the orientation of toroidal moment should be strongly dependent on the mechanical load. Moreover, ambient temperature, boundary conditions and size of the system can strongly affect the relative weights of the components of free energy, thus the combination of these factors and mechanical load should bring more complicated vortex domain patters. These issues need further investigations in the future.

## Methods

**Phase field simulation on ferroelectric nanoplatelet.** In the phase field simulation, the domain structure of a ferroelectric is described by the order parameter, i.e., the spontaneous polarization $\mathbf{P} = (P_1, P_2, P_3)$. The electric displacement field is expressed in terms of electric field, linear induced polarization and nonlinear spontaneous polarization as $\mathbf{D} = \boldsymbol{\varepsilon}_0\mathbf{E} + \boldsymbol{\chi}_b\mathbf{E} + \mathbf{P} = \boldsymbol{\varepsilon}_b\mathbf{E} + \mathbf{P}$, where $\mathbf{E} = -\nabla\varphi$ is the electric field, $\varphi$ is the electric potential, $\boldsymbol{\chi}_b$ is the background susceptibility tensor, $\boldsymbol{\varepsilon}_0$ is the vacuum permittivity, and $\boldsymbol{\varepsilon}_b = \boldsymbol{\varepsilon}_0 + \boldsymbol{\chi}_b$ is the dielectric constant tensor of background material[38-40]. Since the background material is in cubic paraelectric phase, the background dielectric constants along the three axis directions are the same, i.e., $\varepsilon_b = \varepsilon_{11b} = \varepsilon_{22b} = \varepsilon_{33b}$.

The evolution of polarization field toward its equilibrium distribution is driven by the decrease of total free energy of the system, which is phenomenologically described by the time-dependent Ginzburg–Landau (TDGL) equations, i.e.,

$$\frac{\partial P_i}{\partial t} = -M\frac{\delta F}{\delta P_i},\ (i=1,\ 2,\ 3) \tag{1}$$

where $F$ is the total free energy, $M$ the kinetic coefficient related to the domain wall mobility and $t$ the time.

Based on the phenomenological theory, the total free energy of the system is expressed as a functional of order parameter field and applied fields. For the FNPL considered here, taking into account effects of mechanical stress, electric field, surface and spatial polarization variation, the total Gibbs free energy could be written as sum of the Landau free energy $F_{\text{Land}}$, elastic energy $F_{\text{elas}}$, gradient energy $F_{\text{grad}}$, electrostatic energy $F_{\text{elec}}$ and surface energy $F_{\text{surf}}$, that is,

$$\begin{aligned} F &= F_{\text{Land}} + F_{\text{elas}} + F_{\text{grad}} + F_{\text{elec}} + F_{\text{surf}} \\ &= \int_V \left(f_{\text{Land}} + f_{\text{elas}} + f_{\text{grad}} + f_{\text{elec}}\right)dV + \int_S f_{\text{surf}}\,dS \end{aligned} \tag{2}$$

where $f_{\text{Land}}, f_{\text{elas}} f_{\text{grad}}, f_{\text{elec}}$ and $f_{\text{surf}}$ are the corresponding free energy densities, $V$ and $S$ the volume and surface of the FNPL.

For perovskite ferroelectrics, the Landau free energy density $f_{\text{Land}}$ can be generally expressed up to eight-order polynomial expansion for a zero stress as[41-44],

$$\begin{aligned} f_{\text{Land}} = {} & a_1\sum_i P_i^2 + a_{11}\sum_i P_i^4 + a_{12}\sum_{i>j} P_i^2P_j^2 + a_{111}\sum_i P_i^6 + a_{112}\sum_{i>j}\left(P_i^4P_j^2 + P_j^4P_i^2\right) \\ & + a_{123}\prod_i P_i^2 + a_{1111}\sum_i P_i^8 + a_{1112}\sum_{i>j}\left(P_i^6P_j^2 + P_j^6P_i^2\right) \\ & + a_{1122}\sum_{i>j} P_i^4P_j^4 + a_{1123}\sum_{i\neq j\neq k, j>k} P_i^4P_j^2P_k^2 \end{aligned} \tag{3}$$

where $a_i$, $a_{ij}$, $a_{ijk}$ and $a_{ijkl}$ are dielectric stiffness and higher order coefficients fitted to bulk properties.

Under the condition of applied stress, the mechanical stress field (applied and internal) and its coupling with polarization contribute to the elastic energy density, which is described by,

$$f_{\text{elas}} = -Q_{ijkl}\sigma_{ij}P_kP_l - \frac{1}{2}s_{ijkl}\sigma_{ij}\sigma_{kl}, \tag{4}$$

where $s_{ijkl}$ and $Q_{ijkl}$ are the fourth-rank elastic compliance and electrostrictive coefficients, respectively. $\sigma_{ij}$ are stress field components caused by the incompatibility of eigenstrains and external mechanical load. In the absence of body forces, $\sigma_{ij}$ are determined by the mechanical equilibrium equations $\sigma_{ij,j}|_V = 0$ and corresponding mechanical boundary condition $\tau_k|_S = n_i\sigma_{ik}|_S$, where the comma in the subscript denotes spatial differentiation, $\tau_k$ are the surface tractions and $n_i$ the $i$th component of the unit vector normal to the surface.

The spatial polarization variation contributes a gradient energy to the total free energy. To the lowest order of Taylor expansion, the gradient energy density takes the form as $f_{\text{grad}} = \frac{1}{2}G_{ijkl}P_{i,j}P_{k,l}$, with $G_{ijkl}$ being the fourth-rank gradient energy coefficients. Due to truncation at the surface of nanoplatelet, the spontaneous polarization is inhomogeneous across the out-of-plane direction. Thus an additional surface energy is necessary to describe this intrinsic effect. Using the so-called extrapolation length[45], the surface energy density of the ferroelectric nanoplatelet can be approximately given by $f_{\text{surf}} = \frac{1}{2}D_i^SP_i^2/\delta_i^{\text{eff}}$, where $\delta_i^{\text{eff}}$ are extrapolation length and $D_i^S$ the material coefficients related to the gradient energy coefficients and the surface orientation. According to the previous works[38,39,46], the electric energy density of a given polarization distribution is written as $f_{\text{elec}} = -P_iE_i - \frac{1}{2}\varepsilon_bE_iE_i$. In the absence of external electric field, the total electric field is equal to depolarization field induced by spatial polarization variation and incomplete screening of the polarization charges at truncated surfaces. Under the open-circuit condition, for a free-charge-absent body the depolarization field can be calculated by the electrostatic equilibrium equation $D_{i,i}|_V = 0$ and the corresponding boundary condition $D_in_i|_S = 0$.

Ferroelectric phase transition involves structural changes and results spontaneous strains. At stress-free state, these strains are called eigenstrains, which are related to the polarization as $\varepsilon_{ij}^0 = Q_{ijkl}P_kP_l$. Considering the eigenstrains, the stress fields are given by

$$\sigma_{ij} = c_{ijkl}e_{kl} = c_{ijkl}\left(\varepsilon_{kl} - \varepsilon_{kl}^0\right) \tag{5}$$

where $e_{kl}$ are the elastic strains and $\varepsilon_{kl}$ the total strains, which must be compatible and are related to the displacement as $\varepsilon_{ij} = \frac{1}{2}\left(u_{i,j} + u_{j,i}\right)$.

Substitute Eq. (5) into the mechanical equilibrium equations and its boundary condition, we have

$$\begin{cases} c_{ijkl}u_{k,lj}\big|_V = c_{ijkl}\varepsilon_{kl,j}^0\big|_V \\ \tau_j\big|_S = n_ic_{ijkl}\left(u_{k,l} - \varepsilon_{kl}^0\right)\big|_S \end{cases} \tag{6}$$

Similarly, we have the electrostatic equilibrium equation and its boundary condition in term of the potential as

$$\begin{cases} \varepsilon_b\varphi_{,ii}\big|_V = P_{i,i}\big|_V \\ \varepsilon_b\varphi_{,i}n_i\big|_S = P_in_i\big|_S \end{cases} \tag{7}$$

Phase-field simulations are conducted by numerically solving the TDGL Eq. (1) together with the mechanical and electrostatic equilibrium Eqs. (6) and (7). The TDGL equations are solved using the finite difference method, whereas the mechanical and electrostatic equilibrium equations are solved by the finite element method. The time step is chosen to be $\Delta t = 0.01a_0M$, with $a_0 = |a_1|_{T=300K}$. Values of the expansion coefficients of the Landau-potential, electrostrictive coefficients, elastic properties in calculations are listed Table 1. For $PbTiO_3$, a commonly used six-order Landau-potential is adopted in this study.

**Finite element method to solve mechanical and electrostatic model.** In our phase field simulation, the inhomogeneous mechanical stress and electric fields are solved using the finite element method. According to the variation relationship, the mechanical and electrostatic equilibrium equations, i.e., Eqs. (6) and (7), can be solved by finding the extreme value of following functionals, i.e.,

$$I_{\text{elas}}(u_i) = \iiint_V \frac{1}{2}c_{ijkl}\left(\varepsilon_{ij} - \varepsilon_{ij}^0\right)\left(\varepsilon_{kl} - \varepsilon_{kl}^0\right)dV - \iint_S \tau_iu_i\,dS \tag{8a}$$

$$I_{\text{elec}}(\varphi) = \iiint_V \left(\varepsilon_b\varphi_{,i}\varphi_{,i} + 2\varphi P_{i,i}\right)dV - 2\iint_S \varphi P_in_i\,dS \tag{8b}$$

Table 1 | Values of parameter used in the phase-field simulations (SI units and $T$ in K)

| Parameter | Value | Unit |
|---|---|---|
| $a_1$ | $3.85(T-752)\times10^5$ | $C^{-2}m^2N$ |
| $a_{11}$ | $-7.3\times10^7$ | $C^{-4}m^6N$ |
| $a_{12}$ | $7.5\times10^8$ | $C^{-4}m^6N$ |
| $a_{111}$ | $2.6\times10^8$ | $C^{-6}m^{10}N$ |
| $a_{112}$ | $6.1\times10^8$ | $C^{-6}m^{10}N$ |
| $a_{123}$ | $-3.7\times10^9$ | $C^{-6}m^{10}N$ |
| $s_{11}$ | $8.0\times10^{-12}$ | $m^2N^{-1}$ |
| $s_{12}$ | $-2.5\times10^{-12}$ | $m^2N^{-1}$ |
| $s_{44}$ | $9.0\times10^{-12}$ | $m^2N^{-1}$ |
| $Q_{11}$ | 0.089 | $C^{-2}m^4$ |
| $Q_{12}$ | −0.026 | $C^{-2}m^4$ |
| $Q_{44}$ | 0.0675 | $C^{-2}m^4$ |
| $G_{11}$ | $3.46\times10^{-10}$ | $m^4NC^{-2}$ |
| $G_{12}$ | 0 | $m^4NC^{-2}$ |
| $G_{44}$ | $1.73\times10^{-10}$ | $m^4NC^{-2}$ |
| $G'_{44}$ | $1.73\times10^{-10}$ | $m^4NC^{-2}$ |
| $D_i^S$ | $3.46\times10^{-10}$ | $m^4NC^{-2}$ |
| $\delta_i^{eff}$ | $5\times10^{-9}$ | m |
| $\varepsilon_b$ | $4.425\times10^{-10}$ | $Fm^{-1}$ |

Values of the expansion coefficients of the Landau potential, elastic compliance and electrostrictive coefficients are from ref. 42, the isotropic gradient coefficients are from ref. 47, the extrapolation length is from ref. 48, and the background dielectric constant is from ref.38 and 39.

where the freedoms of the two functionals are the displacement $u_i$ and the electric potential $\varphi$, respectively.

In the following, it is convenient to rewrite Eqs. (8) into matrix form, i.e.,

$$\begin{aligned} I_{\text{elas}}(u_i) &= \iiint_V \frac{1}{2}\left(\{\varepsilon\}-\{\varepsilon^0\}\right)^T[C]\left(\{\varepsilon\}-\{\varepsilon^0\}\right)dV - \iint_S \{\tau\}^T\{u\}dS \\ &= \iiint_V \frac{1}{2}\left([L_u]\{u\}-[Q]\{P^2\}\right)^T[C]\left([L_u]\{u\}-[Q]\{P^2\}\right)dV - \iint_S \{\tau\}^T\{u\}dS \end{aligned} \tag{9a}$$

$$\begin{aligned} I_{\text{elec}} &= \iiint_V \left(\varepsilon_b\{\nabla\varphi\}^T\{\nabla\varphi\}+2\varphi P_{i,i}\right)dV - 2\iint_S \varphi P_i n_i dS \\ &= \iiint_V \left[\varepsilon_b\left(\{L_\varphi\}\varphi\right)^T\left(\{L_\varphi\}\varphi\right)+2\varphi P_{i,i}\right]dV - 2\iint_S \varphi P_i n_i dS \end{aligned} \tag{9b}$$

with some vectors and matrices defined as follows,

$$\{u\}=\begin{Bmatrix}u_1\\u_2\\u_3\end{Bmatrix},\quad \{\tau\}=\begin{Bmatrix}\tau_1\\\tau_2\\\tau_3\end{Bmatrix},\quad \{\nabla\varphi\}=\begin{Bmatrix}\frac{\partial\varphi}{\partial x}\\\frac{\partial\varphi}{\partial y}\\\frac{\partial\varphi}{\partial z}\end{Bmatrix},\quad \{\sigma\}=\begin{Bmatrix}\sigma_{11}\\\sigma_{22}\\\sigma_{33}\\\sigma_{23}\\\sigma_{13}\\\sigma_{12}\end{Bmatrix},\quad \{\varepsilon\}=\begin{Bmatrix}\varepsilon_{11}\\\varepsilon_{22}\\\varepsilon_{33}\\2\varepsilon_{23}\\2\varepsilon_{13}\\2\varepsilon_{12}\end{Bmatrix},$$

$$\{\varepsilon^0\}=\begin{Bmatrix}\varepsilon^0_{11}\\\varepsilon^0_{22}\\\varepsilon^0_{33}\\2\varepsilon^0_{23}\\2\varepsilon^0_{13}\\2\varepsilon^0_{12}\end{Bmatrix},\quad \{P^2\}=\begin{Bmatrix}P_1^2\\P_2^2\\P_3^2\\P_2P_3\\P_1P_3\\P_1P_2\end{Bmatrix},\quad \{L_\varphi\}=\begin{Bmatrix}\frac{\partial}{\partial x}\\\frac{\partial}{\partial y}\\\frac{\partial}{\partial z}\end{Bmatrix},$$

$$[L_u]^T=\begin{bmatrix}\frac{\partial}{\partial x}&0&0&0&\frac{\partial}{\partial z}&\frac{\partial}{\partial y}\\0&\frac{\partial}{\partial y}&0&\frac{\partial}{\partial z}&0&\frac{\partial}{\partial x}\\0&0&\frac{\partial}{\partial z}&\frac{\partial}{\partial y}&\frac{\partial}{\partial x}&0\end{bmatrix},$$

$$[C]=\begin{bmatrix}c_{11}&c_{12}&c_{12}&0&0&0\\c_{12}&c_{11}&c_{12}&0&0&0\\c_{12}&c_{12}&c_{11}&0&0&0\\0&0&0&c_{44}&0&0\\0&0&0&0&c_{44}&0\\0&0&0&0&0&c_{44}\end{bmatrix}\text{ and }[Q]=\begin{bmatrix}Q_{11}&Q_{12}&Q_{12}&0&0&0\\Q_{12}&Q_{11}&Q_{12}&0&0&0\\Q_{12}&Q_{12}&Q_{11}&0&0&0\\0&0&0&Q_{44}&0&0\\0&0&0&0&Q_{44}&0\\0&0&0&0&0&Q_{44}\end{bmatrix} \tag{10}$$

In the finite element method of this study, the simulated ferroelectric is meshed into eight-node cubic elements. The displacement vector and the electric potential at the $i$th nodes of an element are denoted as $\{\delta_i\}=\{u_1^i u_2^i u_3^i\}$ and $\varphi_i$, with $i = 1, 2, 3, \ldots, 8$. The displacement vector and the electric potential of the eight nodes in each element is then expressed by column vectors as

$$\{\delta^e\}=\{\{\delta_1\}\{\delta_2\}\{\delta_3\}\{\delta_4\}\{\delta_5\}\{\delta_6\}\{\delta_7\}\{\delta_8\}\}^T \tag{11a}$$

$$\{\varphi^e\}=\{\varphi_1\varphi_2\varphi_3\varphi_4\varphi_5\varphi_6\varphi_7\varphi_8\}^T \tag{11b}$$

The displacement and the electric potential in the element are expressed in terms of those of the nodes, i.e.,

$$\{u\}=[N_u]\{\delta^e\}\text{ and }\varphi=[N_\varphi]\{\varphi^e\} \tag{12}$$

in which

$$[N_u]=\begin{bmatrix}N_{u1}&0&0&N_{u2}&0&0&\cdots&N_{u8}&0&0\\0&N_{u1}&0&0&N_{u2}&0&\cdots&0&N_{u8}&0\\0&0&N_{u1}&0&0&N_{u2}&\cdots&0&0&N_{u8}\end{bmatrix} \tag{13}$$

and

$$[N_\varphi]=[N_{\varphi1}N_{\varphi2}\cdots N_{\varphi8}] \tag{14}$$

where $N_{ui}$ and $N_{\varphi i}$ are the interpolation functions.

Substitute Eqs. (12) into Eqs. (9), we have,

$$\begin{aligned} I_{\text{elas}} &= \sum_e \iiint_{V_e} \frac{1}{2}\left([B_u]\{\delta^e\}-[Q]\{P^2\}\right)^T[C]\left([B_u]\{\delta^e\}-[Q]\{P^2\}\right)dV \\ &- \sum_{e'} \iint_{S_e} \{\tau\}^T[N_u]\{\delta^e\}dS \end{aligned} \tag{15a}$$

$$\begin{aligned} I_{\text{elec}} &= \sum_e \iiint_{V_e} \left[\varepsilon_b\left([B_\varphi]\{\varphi^e\}\right)^T\left([B_\varphi]\{\varphi^e\}\right)+2P_{i,i}[N_\varphi]\{\varphi^e\}\right]dV \\ &- \sum_{e'} 2\iint_{S_e} P_i n_i[N_\varphi]\{\varphi^e\}dS \end{aligned} \tag{15b}$$

where $e$ and $e$' label the elements in the volume and those at the surface, respectively, matrices $[B_u]\equiv[L_u][N_u]$ and $[B_\varphi]\equiv[L_\varphi][N_\varphi]$.

Variation of the two functionals in Eqs. (15) with respect to the displacement $\{\delta^e\}$ and the electric potential $\{\varphi^e\}$ at all nodes should be zero, which results

$$\begin{aligned} \delta I_{\text{elas}} &= \sum_e \iiint_{V_e} \left([B_u]\{\delta^e\}-[Q]\{P^2\}\right)^T[C][B_u]\delta\{\delta^e\}dV \\ &- \sum_{e'} \iint_{S_e} \{\tau\}^T[N_u]\delta\{\delta^e\}dS=0 \end{aligned} \tag{16a}$$

$$\begin{aligned} \delta I_{\text{elec}} &= \sum_e 2\iiint_{V_e} \left[\varepsilon_b\{\varphi^e\}^T[B_\varphi]^T[B_\varphi]+P_{i,i}[N_\varphi]\right]\delta\{\varphi^e\}dV \\ &- \sum_e 2\iint_{S_e} P_i n_i[N_\varphi]\delta\{\varphi^e\}dS=0 \end{aligned} \tag{16b}$$

Based on the variation principle, the following element equations can be obtained from Eqs. (16), i.e.,

$$[K_u^e]\{\delta^e\}=\{F_u^e\}\text{ and }[K_\varphi^e]\{\varphi^e\}=\{F_\varphi^e\} \tag{17}$$

where

$$[K_u^e]=\iiint_{V_e}[B_u]^T[C][B_u]dV \tag{18a}$$

$$[K_\varphi^e]=\iiint_{V_e}\varepsilon_b[B_\varphi]^T[B_\varphi]dV \tag{18b}$$

$$\{F_u^e\}=\iiint_{V_e}[B_u]^T[C][Q]\{P^2\}dV+\iint_{S_e}[N_u]^T\{\tau\}dS \tag{18c}$$

$$\{F_\varphi^e\}=\iiint_{V_e}P_{i,i}[N_\varphi]^TdV+\iint_{S_e}P_i n_i[N_\varphi]^TdS \tag{18d}$$

are the stiffness matrices and node force vectors of element e. Assembling the stiffness matrices, displacement and electric potential vector, and the force vectors of all the elements together yields the global equations:

$$[K_u]\{U\} = \{F_u\} \text{ and } [K_\varphi]\{\varphi\} = \{F_\varphi\} \quad (19)$$

where $[K_u]$ and $[K_\varphi]$ are global stiffness matrices, $\{F_u\}$ and $\{F_\varphi\}$ are global force vectors, and $\{U\}$ and $\{\Phi\}$ are the vectors containing all the node displacement and electric potential, respectively. The node displacement and electric potential can be conveniently determined by solving Eqs. (19) using the Gauss-Seidel iteration method.


1. Scott, J. F. Nanoferroelectrics: statics and dynamics. *J. Phys.: Condens. Matter* **18**, R361 (2006).
2. Rørvik, P. M., Grande, T. & Einarsrud, M.-A. One-dimensional nanostructures of ferroelectric perovskites. *Adv. Mater.* **23**, 4007–4034 (2011).
3. Zhuravlev, M. Y., Sabirianov, R. F., Jaswal, S. S. & Tsymbal, E. Y. Giant electroresistance in ferroelectric tunnel junctions. *Phys. Rev. Lett.* **94**, 246802 (2005).
4. Zheng, Y., Zheng, Y., Woo, C. H. & Wang B. Pulse-loaded ferroelectric nanowire as an alternating current source. *Nano Lett.* **8**, 3131–3136 (2008).
5. Xu, S., Hansen, B. J. & Wang, Z. L. Piezoelectric-nanowire-enabled power source for driving wireless microelectronics. *Nat. Commun.* **1**, 93 (2010).
6. Yang, S. Y. *et al*. Above-bandgap voltages from ferroelectric photovoltaic devices. *Nat. Nanotech.* **5**, 143–147 (2010).
7. Zheng, Y. & Woo, C. H. Giant piezoelectric resistance in ferroelectric tunnel junctions. *Nanotechnology* **20**, 075401 (2009).
8. Luo, X., Wang, B. & Zheng, Y. Tunable tunneling electroresistance in ferroelectric tunnel junctions by mechanical loads. *ACS Nano* **5**, 1649–1656 (2011).
9. Cao, S. *et al*. Extreme chemical sensitivity of nonlinear conductivity in charge-ordered $LuFe_2O_4$. *Scientific Report* **2**, 330 (2012).
10. Fu, H. & Bellaiche, L. Ferroelectricity in barium titanate quantum dots and wires. *Phys. Rev. Lett.* **91**, 257601 (2003).
11. Naumov, I. I., Bellaiche, L. & Fu, H. Unusual phase transitions in ferroelectric nanodisks and nanorods. *Nature* **432**, 737–740 (2004).
12. Naumov, I. & Bratkovsky, A. M. Unusual polarization patterns in flat epitaxial ferroelectric nanoparticles. *Phys. Rev. Lett.* **101**, 107601 (2008).
13. Prosandeev, S., Ponomareva, I., Naumov, I., Kornev, I. & Bellaiche, L. Original properties of dipole vortices in zero-dimensional ferroelectrics. *J. Phys.: Condens. Matter* **20**, 193201 (2008).
14. Gruverman, A. *et al*. Vortex ferroelectric domains. *J. Phys.: Condens. Matter* **20**, 342201 (2008).
15. Prosandeev, S. & Bellaiche, L. Hypertoroidal moment in complex dipolar structures. *J. Mater. Sci.* **44**, 5235–5248 (2009).
16. Hong, J. *et al*. Topology of the polarization field in ferroelectric nanowires from first principles. *Phys. Rev. B* **81**, 172101 (2010).
17. Schilling, A. *et al*. Domains in ferroelectric nanodots. *Nano Lett.* **9**, 3359-3364 (2009).
18. Rodriguez, B. J. *et al*. Vortex polarization states in nanoscale ferroelectric arrays. *Nano Lett.* **9**, 1127–1131 (2009).
19. Ivry, Y., Chu, D. P., Scott, J. F. & Durkan, C. Flux closure vortexlike domain structures in ferroelectric thin films. *Phys. Rev. Lett.* **104**, 207602 (2010).
20. McGilly, L. J., Schilling, A. & Gregg, J. M. Domain bundle boundaries in single crystal $BaTiO_3$ lamellae: searching for naturally forming dipole flux-closure/quadrupole chains. *Nano Lett.* **10**, 4200–4205 (2010).
21. Stachiotti, M. G. & Sepliarsky, M. Toroidal ferroelectricity in $PbTiO_3$ nanoparticles. *Phys. Rev. Lett.* **106**, 137601 (2011).
22. Nelson, C. T. *et al*. Spontaneous vortex nanodomain arrays at ferroelectric heterointerfaces. *Nano Lett.* **11**, 828–834 (2011).
23. McGilly, L. J. & Gregg, J. M. Polarization closure in $PbZr_{(0.42)}Ti_{(0.58)}O_3$ nanodots. *Nano Lett.* **11**, 4490–4495 (2011).
24. McQuaid, R. G. P. *et al*. Mesoscale flux-closure domain formation in single-crystal $BaTiO_3$. *Nat. Commun.* **2**, 404 (2011).
25. Balke, N. *et al*. Enhanced electric conductivity at ferroelectric vortex cores in $BiFeO_3$. *Nature Phys.* **8**, 81–88 (2011).
26. Jia, C. L., Urban, K. W., Alexe, M., Hesse, D. & Vrejoiu, I. Direct observation of continuous electric dipole rotation in flux-closure domains in ferroelectric $Pb(Zr,Ti)O_3$. *Science* **331**, 1420–1423 (2011).
27. Schilling, A. *et al*. Shape-induced phase transition of domain patterns in ferroelectric platelets. *Phys. Rev. B* **84**, 064110 (2011).
28. Catalan, G., Seidel, J., Ramesh, R. & Scott, J. F. Domain wall nanoelectronics. *Rev. Mod. Phys.* **84**, 119–156 (2012).
29. Ponomareva, I., Naumov, I. & Bellaiche, L. Low-dimensional ferroelectrics under different electrical and mechanical boundary conditions: Atomistic simulations. *Phys. Rev. B* **72**, 214118 (2005).
30. Prosandeev, S. & Bellaiche, L. Characteristics and signatures of dipole vortices in ferroelectric nanodots: first-principles-based simulations and analytical expressions. *Phys. Rev. B* **75**, 094102 (2007).
31. Prosandeev, S., Ponomareva, I., Kornev, I., Naumov, I. & Bellaiche, L. *Phys. Rev. Lett.* Controlling toroidal moment by means of an inhomogeneous static field: an *ab* initio study. **96**, 237601 (2006).
32. Naumov, I. & Fu, H. Vortex-to-polarization phase transformation path in ferroelectric $Pb(ZrTi)O_3$ nanoparticles. *Phys. Rev. Lett.* **98**, 077603 (2007).
33. Prosandeev, S., Ponomareva, I., Kornev, I. & Bellaiche, L. Control of vortices by homogeneous fields in asymmetric ferroelectric and ferromagnetic rings. *Phys. Rev. Lett.* **100**, 047201 (2008).
34. Prosandeev, S. & Bellaiche, L. Controlling double vortex states in low-dimensional dipolar systems. *Phys. Rev. Lett.* **101**, 097203 (2008).
35. Naumov, I. & Fu, H. Cooperative response of $Pb(ZrTi)O_3$ nanoparticles to curled electric fields. *Phys. Rev. Lett.* **101**, 197601 (2008).
36. Wang, J. Switching mechanism of polarization vortex in single-crystal ferroelectric nanodots. *Appl. Phys. Lett.* **97**, 192901 (2010).
37. Chen, W. J., Zheng, Y. & Wang, B. Phase field simulations of stress controlling the vortex domain structures in ferroelectric nanosheets. *Appl. Phys. Lett.* **100**, 062901 (2012).
38. Zheng, Y. & Woo, C. H. Thermodynamic modeling of critical properties of ferroelectric superlattices in nano-scale. *Appl. Phys. A: Mater. Sci. Process.* **97**, 617–626 (2009).
39. Woo, C. H. & Zheng, Y. Depolarization in modeling nano-scale ferroelectrics using the Landau free energy functional. *Appl. Phys. A: Mater. Sci. Process.* **91**, 59–63 (2008).
40. Tagantsev, A. K. Landau Expansion for Ferroelectrics: Which Variable to Use? *Ferroelectrics* **375**, 19–27 (2008).
41. Haun, M. J., Furman, E., Jang, S. J., McKinstry, H. A. & Cross, L. E. Thermodynamic theory of $PbTiO_3$. *J. Appl. Phys.* **62**, 3331 (1987).
42. Pertsev, N. A., Zembilgotov, A. G. & Tagantsev, A. K. Effect of Mechanical Boundary Conditions on Phase Diagrams of Epitaxial Ferroelectric Thin Films. *Phys. Rev. Lett.* **80**, 1988 (1998).
43. Li, Y. L., Cross, L. E. & Chen, L. Q. A phenomenological thermodynamic potential for $BaTiO_3$ single crystals. *J. Appl. Phys.* **98**, 064101 (2005).
44. Wang, Y. L. *et al*. Anharmonicity of $BaTiO_3$ single crystals. *Phys. Rev. B* **73**, 132103 (2006).
45. Kretschmer, R. & Binder, K. Surface effects on phase transitions in ferroelectrics and dipolar magnets. *Phys. Rev. B* **20**, 1065 (1979).
46. Landau, L. D., Lifshitz, E. M. & Pitaevskii, L. P. *Electrodynamics of continuous media*, Oxford University Press: New York, (1984).
47. Li,Y. L. *et al*. Effect of electrical boundary conditions on ferroelectric domain structures in thin films. *Appl. Phys. Lett.* **81**, 427 (2002).
48. Ishikawa, K. & Uemori, T. Surface relaxation in ferroelectric perovskites. *Phys. Rev. B* **60**, 11841 (1999).


## Acknowledgements

Helpful discussions with Dr. D. C. Ma and Dr. S. P. Lin are gratefully acknowledged. The authors also acknowledge the financial support of the National Natural Science Foundation of China (NSFC) (Nos. 10902128, 11232015, 50802026, 10972239). Y. Z. also thanks support by the Fundamental Research Funds for the Central Universities to Micro&Nano Physics and Mechanics Research Laboratory, and New Century Excellent Talents in University, Research Fund for the Doctoral Program of Higher Education, and Fok Ying Tung Foundation.

## Author contributions

Y. Z. initiated and performed this work and manuscript. W. J. C. performed the simulations. B. W. suggested the principle idea. Y. Z. and W. J. C. analyzed the numerical results. W. J. C., Y. Z. and B. W. wrote the manuscript. All authors contributed to discussion and reviewed the manuscript.

## Additional information

**Supplementary information** accompanies this paper at http://www.nature.com/scientificreports

**Competing financial interests:** The authors declare no competing financial interests.



**How to cite this article:** Chen, W.J., Zheng, Y. & Wang, B. Vortex Domain Structure in Ferroelectric Nanoplatelets and Control of its Transformation by Mechanical Load. *Sci. Rep.* **2**, 796; DOI:10.1038/srep00796 (2012).